A&A 667, A165 (2022)
https://doi.org/10.1051/0004-6361/202244578

Astronomy & Astrophysics

JWST/MIRI coronagraphic performances as measured on-sky

A. Boccaletti[1], C. Cossou[2], P. Baudoz[1], P. O. Lagage[2], D. Dicken[3,4], A. Glasse[3,4], D. C. Hines[5], J. Aguilar[5], O. Detre[6], B. Nickson[5], A. Noriega-Crespo[5], A. Gáspár[7], A. Labiano[8,9], C. Stark[10], D. Rouan[1], J. M. Reess[1], G. S. Wright[3], G. Rieke[7], M. Garcia Marin[11], C. Lajoie[5], J. Girard[5], M. Perrin[5], R. Soummer[5], and L. Pueyo[5]

[1] LESIA, Observatoire de Paris, Université PSL, CNRS, Sorbonne Université, Université de Paris Cité, 5 place Jules Janssen, 92195 Meudon, France
e-mail: Anthony.boccaletti@obspm.fr
[2] Université Paris-Saclay, Université Paris Cité, CEA, CNRS, AIM, 91191 Gif-sur-Yvette, France
[3] UKATC, The Royal Observatory, Blackford Hill, Edinburgh, EH9 3HJ, Scotland
[4] Institute for Astronomy, University of Edinburgh, Royal Observatory, Blackford Hill, Edinburgh EH9 3HJ, Scotland
[5] Space Telescope Science Institute, 3700 San Martin Dr, Baltimore, Maryland 21218, USA
[6] Max-Planck-Institut für Astronomie (MPIA), Königstuhl 17, 69117 Heidelberg, Germany
[7] Steward Observatory and the Department of Astronomy, The University of Arizona, 933 N Cherry Ave, Tucson, AZ, 85721, USA
[8] Telespazio UK for the European Space Agency, ESAC, Camino Bajo del Castillo s/n, 28692 Villanueva de la Cañada, Spain
[9] Centro de Astrobiología (CSIC-INTA), Carretera de Ajalvir, 28850 Torrejón de Ardoz, Madrid, Spain
[10] NASA Goddard Space Flight Center, Exoplanets & Stellar Astrophysics Laboratory, Code 667, Greenbelt, MD 20771, USA
[11] European Space Agency, 3700 San Martin Drive, Baltimore, MD21218, USA

Received 22 July 2022 / Accepted 5 September 2022

ABSTRACT

Context. Characterization of directly imaged exoplanets is one of the most eagerly anticipated science functions of the *James Webb* Space Telescope. MIRI, the mid-IR instrument, has the capability to provide unique spatially resolved photometric data points in a spectral range never before achieved for such objects.
Aims. We aim to present the very first on-sky contrast measurements of the MIRI coronagraphs. In addition to a classical Lyot coronagraph at the longest wavelength, this observing mode implements the concept of the four-quadrant phase mask for the very first time in a space telescope.
Methods. We observed single stars together with a series of reference stars to measure raw contrasts as they are delivered on the detector, as well as reference-subtracted contrasts.
Results. The MIRI coronagraphs achieve raw contrasts better than 10^{-3} at the smallest angular separations (within 1″) and about 10^{-5} farther out (beyond 5 ∼ 6″). Subtracting the residual diffracted light left behind the coronagraph has the potential to bring the final contrast down to the background- and detector-limited noise floor at most angular separations (a few times 10^{-5} at less than 1″).
Conclusions. The MIRI coronagraphs behave as expected from simulations. In particular, the raw contrasts for all four coronagraphs are fully consistent with the diffractive model. Contrasts obtained by subtracting reference stars also meet expectations and are fully demonstrated for two four-quadrant phase masks (F1065C and F1140C). The worst contrast, measured at F1550C, is very likely due to a variation in the phase aberrations at the primary mirror during the observations, and not an issue with the coronagraph itself. We did not perform reference star subtraction with the Lyot mask at F2300C, but we anticipate that it would bring the contrast down to the noise floor.

Key words. instrumentation: high angular resolution – techniques: high angular resolution – techniques: image processing – planetary systems

1. Introduction

Exoplanet characterization is entering a new era with the *James Webb* Space Telescope (JWST), in particular with the coronagraphs of the mid-IR instrument MIRI (Rieke et al. 2015; Wright et al. 2015), designed to obtain high contrast imaging of exoplanetary systems at mid-IR wavelengths. To date, several exoplanets have been directly imaged at near-IR, mostly from the ground with adaptive optics facilities, but no observations have been obtained beyond ∼5 µm (with the exception of a candidate detection around α Cen by Wagner et al. 2021). The few observations performed with ground-based instruments at the *M* band are strongly affected by lower sensitivity due to the sky brightness and variability (Stolker et al. 2020).

The MIRI coronagraphic mode is a suite of four focal plane masks (permanently mounted in the imager field of view), each paired with a dedicated filter and an optimized Lyot stop. They were designed to offer large contrasts and, importantly, small inner working angles (IWAs)[1] at mid-IR. Despite longer operating wavelengths than NIRCAM (the near-IR instrument of *James Webb*), the MIRI coronagraphs deliver similar IWAs (∼0.33″ at F1065C). Three of these coronagraphs use four-quadrant phase masks (4QPMs; Rouan et al. 2000), manufactured with reactive ion etching in a germanium

[1] The IWA, although sometimes ill defined, is the angular separation at which an off-axis point source will have its transmission reduced to 50%.

Table 1. Summary of MIRI coronagraphic configurations.

Filter	Coronagraph	Stop [%]	Central wavelength [μm]	Bandwidth [μm]	IWA [″]
F1065C	4QPM_1065	62	10.575	0.75	0.33
F1140C	4QPM_1140	62	11.30	0.80	0.36
F1550C	4QPM_1550	62	15.50	0.90	0.49
F2300C	LYOT_2300	72	22.75	5.50	2.16

substrate. Details about the 4QPM manufacturing for MIRI can be found in Baudoz et al. (2006). Since the 4QPMs are chromatic, they are used in conjunction with the narrow-band filters F1065C ($\lambda_0 = 10.575$ μm, $\Delta\lambda = 0.75$ μm), F1140C ($\lambda_0 = 11.30$ μm, $\Delta\lambda = 0.8$ μm), and F1550C ($\lambda_0 = 15.50$ μm, $\Delta\lambda = 0.9$ μm), mounted in the filter wheel together with a Lyot stop that transmits 62% of the telescope aperture. Because the stop is not just a downsized version of the JWST pupil but has been optimized to attenuate the starlight diffraction, the point spread function (PSF) of an off-axis object is slightly broader than with the full pupil. The field of view (FOV) of the 4QPM subarrays is 24″ × 24″. Another coronagraph that uses a classical Lyot mask with a diameter of $3\lambda/D$, the equivalent of 2.1″, is dedicated to longer wavelength observations with the F2300C filter ($\lambda_0 = 22.75$ μm, $\Delta\lambda = 5.5$ μm). This coronagraph, with a FOV of 30″ × 30″, uses a Lyot stop with a different shape and a transmission of 72%. Pre-flight details about the MIRI coronagraphs can be found in Boccaletti et al. (2015), and Table 1 summarizes the available configurations.

The central wavelengths of the filters were chosen to characterize the atmospheres of directly imaged, young giant exoplanets, essentially to complement near-IR photometric and spectroscopic measurements. The F1065C and F1140C filters are meant to provide photometric measurements of exoplanets in and out of the ammonia absorption band. The F1550C filter, in combination with F1140C, is important for constraining models of the thermal balance of the planet and of the behavior of any atmosphere. The detection performance was first estimated in Boccaletti et al. (2005, 2015). Some recent simulations of planet detection with the MIRI coronagraphs can also be found in Danielski et al. (2018) and Hinkley et al. (2022). The Lyot mask, by design, is not intended to directly image planets (except a few at wide separations, such as HD 106906b), but rather is optimized to detect cold material around bright stars, such as debris disks, which are reminiscent of Kuiper belts in young systems (see for instance Lebreton et al. 2016). The larger FOV in this channel was adopted to include, as far as possible, the outer debris belts of even the most extended systems.

The MIRI coronagraphs were previously tested on the ground, but the performance was strongly disturbed by the strong thermal background and the test bench features, which limit the achievable contrast to a few 10^{-3} (Cavarroc et al. 2008a). The purpose of this paper is to present the actual performance of the MIRI coronagraphs as measured during JWST commissioning and to compare these results to simulations, which were recently revised to include the most relevant knowledge of the telescope and the instrument.

The paper is organized as follows: Sect. 2 describes the observations, and Sect. 3 the simulations. The measured contrasts on-sky are presented in Sect. 4.

2. Observations

Observations were carried out in June 2022. Table 2 provides a list of the data that were used for estimating the contrasts delivered by the MIRI coronagraphs. We selected the targets to avoid saturation when observed off-axis (a few arcseconds away to avoid the attenuation of the coronagraphs) to measure the PSF for a photometric reference, as well as to provide a sufficient flux level compatible with the sensitivity at each filter when the star is on-axis, and hence masked and attenuated by the coronagraph (attenuation on-axis can be as large as a factor of ~400 as measured in F1550C). We ended up with two series of objects, one set optimized for F1065C and F1140C and the other for F1550C and F2300C. The targets are: HD 158165 ($K = 4.07$), of which the flux densities are 0.550 Jy and 0.450 Jy for, respectively, F1065C and F1140C; and HD 163113 ($K = 2.75$), for F1550C and F2300C, with flux densities 1.445 Jy and 0.532 Jy, respectively.

The observations recorded during the commissioning of the MIRI coronagraphs were primarily intended to measure the raw contrasts, which correspond to the starlight attenuation at the detector as a function of angular separation. Raw coronagraphic images in this particular case are entirely dominated by the diffraction of the telescope pupil leaking through the Lyot stop. The residual starlight can be further calibrated and subtracted with the use of reference stars. At this second step, the dominant terms are expected to come from the telescope wavefront errors and their variations in time, as well as the telescope pointing repeatability onto the coronagraph. While a long-term strategy will certainly involve a library of coronagraphic images and dedicated algorithms for post-processing (Choquet et al. 2014), the commissioning procedure makes use of one or two reference stars observed back-to-back with the targets, or a few days apart.

Reference stars were chosen to have similar flux densities in the coronagraphic filters and are located at several distances on the sky to test the effect of telescope slews. The 4QPM/F1140C coronagraph is the one identified to perform most of these tests with reference stars. In the F1140C filter, we observed two reference stars, BD +30 2990 and HD 158896, located respectively at 0.7° and 20.7° from the target. The former was also observed in the F1065C filter. In the F1550C filter, the reference star HD 162989 is at 1.16° from the target. No reference star was observed for the Lyot coronagraph.

Figure 1 shows images of each of the coronagraphic fields when observing the background sky. All four show an unexpected stray light feature, known familiarly as "glow sticks", which appear as increased signal along the structural edges in the MIRI imager entrance focal plane. They are most apparent across the center of the F1550C image, where light is being scattered into the "science" optical path by the raised edge of the phase boundary. In the F2300C image, the bright glow stick marks scattering at the lower edge of the aluminium Lyot aperture. The stray light is visible, but fainter, for the shorter wavelength

Table 2. Main parameters of the observations during the MIRI coronagraph's commissioning.

Date UT	Filter	Object	Type	Obs ID	N_{group}	N_{int}	Dither	T_{exp} per dither (s)
06/09/2022	F1140C	BD +30 2990	REF 1 ON	1037 / obs 4	100	21	9	508.122
06/09/2022	F1140C	HD 158165	TARG ON	1037 / obs 5	100	21	9	508.122
06/09/2022	F1140C	HD 158165	TARG OFF	1037 / obs 6	10	25	4	65.672
06/09/2022	F1140C	HD 158896	REF 10 ON	1037 / obs 7	100	21	9	508.122
06/13/2022	F1140C	–	BGD	1045 / obs 65	100	21	4	508.122
06/20/2022	F1140C	BD +30 2990	REF 1 ON 2nd	1037 / obs 30	100	21	9	508.122
06/18/2022	F1550C	–	BGD	1037 / obs 8	100	95	4	2299.49
06/18/2022	F1550C	HD 163113	TARG OFF	1037 / obs 9	10	25	4	65.672
06/18/2022	F1550C	HD 163113	TARG ON	1037 / obs 10	100	95	9	2299.49
06/18/2022	F1550C	HD 162989	REF 1 ON	1037 / obs 11	100	95	9	2299.49
06/20/2022	F1065C	–	BGD	1037 / obs 26	100	21	4	508.122
06/20/2022	F1065C	HD 158165	TARG OFF	1037 / obs 27	10	25	4	65.672
06/20/2022	F1065C	HD 158165	TARG ON	1037 / obs 28	100	21	9	508.122
06/20/2022	F1065C	BD +30 2990	REF 1 ON	1037 / obs 29	100	21	9	508.122
06/23/2022	F2300C	–	BGD	1037 / obs 32	100	90	4	2944.836
06/23/2022	F2300C	HD 163113	TARG OFF	1037 / obs 33	10	25	4	88.776
06/23/2022	F2300C	HD 163113	TARG ON	1037 / obs 34	100	90	1	2944.836

Notes. Date, filter, name of the object, type of object (target or reference, degrees separation on-sky from the target, on or off the center of the coronagraph, or background image), ID of the program, group number, number of integrations, number of dither positions (9 is for the SGD, 4 or 1 is a classical dither), and total exposure time per dither.

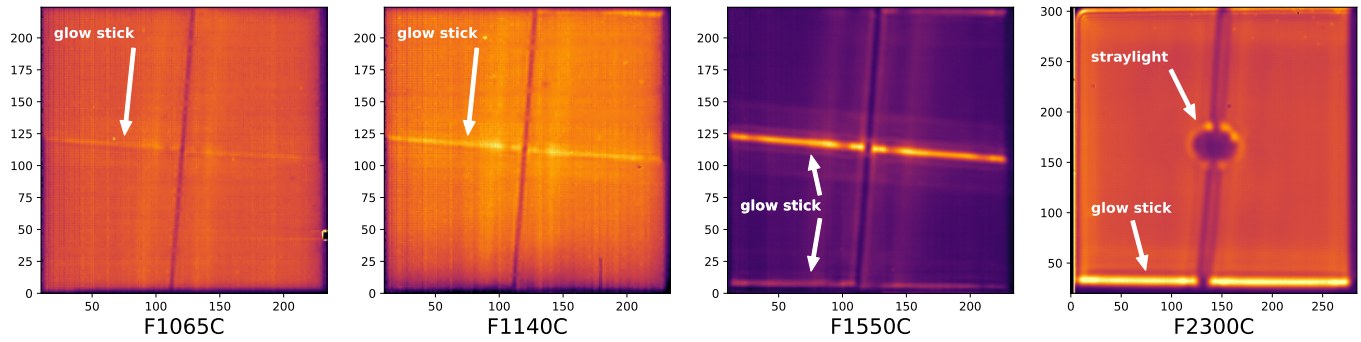

Fig. 1. Images of the background obtained in the coronagraphic subarrays showing the "glow sticks" visible at the horizontal transitions of the 4QPMs and around the disk of the Lyot mask, as well as at the edges of the coronagraphs' support structure. The intensity scale is linear and is adapted for each image for visualization purposes.

4QPM coronagraphs in Fig. 1. Stray light is also seen along the upper edge of the Lyot spot.

Two key observations were important in determining the root cause of the glow sticks. First, their shape and brightness were independent of the observatory pointing direction to within a few percent, ruling out an astronomical origin. Second, photometric analysis of the glow sticks determined that the illuminating source was well fitted by a gray body spectrum with an effective temperature of 120 ± 20 K, characteristic of the region where the sunshield approaches the deployable tower assembly (Lightsey et al. 2012). Nonsequential optical path analysis (S. Rohrbach, priv. comm.) has used the pre-launch solid model of the observatory plus MIRI to identify a path from this warm region of the sunshield to the MIRI entrance focal plane, via a reflection from the secondary mirror (SM), followed by scattering from the hinged SM support strut. The model reproduces features similar to the glow sticks by modeling the scattering process at the mechanical edges of the phase masks and Lyot stop. The agreement is not yet perfect: the model produces glow sticks along both the vertical and horizontal nulling axes of the phase masks, whereas we only observe features in the horizontal (along row) direction in our data. We ascribe this discrepancy to a lack of fidelity between the pre-launch solid model and the as-flown hardware.

To mitigate the glow stick effect (which could be brighter than the observed source itself), it is necessary to subtract a background image obtained in the same filter and for an identical exposure time until the variability of this pattern is understood and an alternative approach is proposed. If this procedure is followed, the effect of the glow sticks on the final data is completely removed, except for the expected modest increase in photon noise at their positions. At the moment, this step is not automatically included in the observing sequence, nor in the reduction pipeline.

To precisely center the star on the coronagraph axis, we need both a sub-pixel estimation of the coronagraph position and a precise target acquisition (TA) procedure (Cavarroc et al. 2008b). The glow sticks prevented us from using the dark

Table 3. Three input cases used to simulate the performance of the MIRI coronagraphs.

	OPD tel. [nm]	OPD MIRI [nm]	OPD Frill [nm]	OPD IEC [nm]	OPD TD [nm]	TA [mas axis^{-1}]	Jitter [mas axis^{-1}]	Pupil shear [%]
Best	73	32	0.017	1.6	0.016	6.25	2.5	0
Nominal	73	32	0.07	2.8	0.07	8.76	3.8	2
Requirement	73	32	1.75	4.6	1.67	12.51	5.8	4

Notes. Wavefront errors (OPD) are provided in nanometers RMS from the telescope, the instrument MIRI, the frill around the primary mirror, the ISIM electronics compartment (IEC), and thermal distortion (TD), respectively. TA and jitter are given in milliarcsec per axis, and the shear is given as a percentage of the telescope pupil.

transitions of the 4QPMs to estimate the coronagraph center, which had been the plan. Instead, we developed a method based on comparison with a diffraction model after subtracting the glow sticks out, to be presented in a separate paper (Baudoz et al., in prep.). These measurements were used in the TA procedure to reach a pointing accuracy of about 5 to 10 mas, in full agreement with the requirement (Rigby et al. 2022).

3. Simulations

The simulations presented in Boccaletti et al. (2015) were recently reassessed by the JWST Coronagraph Sensitivity Working Group to incorporate the up-to-date telescope and instrument parameters. We assumed a temporal sampling of $\pi/5 \approx 0.63$ min per frame, for a total sequence of about 56 min on the target (90 frames) followed by the same amount of telescope time on a reference star, which is dithered on nine positions (9×10 frames, i.e., each dither position has a total of one-ninth the exposure time as the target source.). This so-called small grid dither (SGD; Soummer et al. 2014; Lajoie et al. 2016) allows a diversity in the observations of the reference star to further reduce the starlight, making use, for instance, of principal component analysis (PCA; Soummer et al. 2012). The SGD is a square grid with 10 mas steps. Although the error on the positioning of the star onto this grid is estimated to be 1 or 2 mas, this has no effect on the estimation of the starlight, which only relies on the variations in the intensity of speckles around the mask center, not on absolute knowledge of the pointing.

Static aberrations include the telescope wavefront aberration as measured in the early phase of commissioning (73 nm RMS) and the MIRI instrument aberrations measured on the ground (32 nm RMS). The former wavefront map is made of mid spatial frequencies and is expected to evolve over the life of the mission, while the latter contains mostly low spatial frequencies. Additional dynamical components in the wavefront on a $\sim$1−2 h timescale are also taken into account with various spatial and temporal frequencies, such as the thermal distortion of the telescope backplane, the fast oscillation in the heaters in the Integrated Science Instruments Module (ISIM) electronics compartment, and the frill around the primary mirror designed to stop the stray light, all being relatively small in terms of wavefront errors for an instrument such as MIRI (Table 3).

In addition, the simulation accounts for misalignments at the focal plane and pupil plane in the coronagraph. First of all, the offset between the star's position and the center of the mask corresponds to the TA error. For convenience, in the simulations the target star is perfectly centered while the reference star is offset by this TA error. Then, we included line of sight jitter that is the motion of the star's position during the observation. Moreover, the Lyot stop, located at the MIRI filter wheel, can be slightly misaligned with the telescope pupil. This error is expressed as a percentage of the telescope pupil diameter, assuming a shear along the diagonal. Three distinct scenarios were considered: "best", "nominal", and "requirement". The values for all parameters of the simulations are provided in Table 3. Finally, we included a spectral shift of 3% of the F1140C filter with respect to the operating wavelength of the corresponding 4QPM, which caused a chromatic leakage in the images visible as a central peak in the coronagraphic image.

The simulations are time averaged, so we are left with one single image for the target and nine for the reference. We applied PCA using nine components to build a reference frame and then subtracted this out from the target image. We provide a comparison of the PSF images (off-axis) and coronagraphic images (on-axis) observed during commissioning to simulated images in Figs. 2 and 3, respectively. They are virtually identical, and the surrounding field on the observed image is very clean, with no evidence of residual latent images.

4. Measured contrasts

The data were processed with the dedicated JWST pipeline up to stage 1, which involved detector-level corrections (`calwebb_detector1`; see JWST pipeline documentation) and produced level 2a count-rate data, but without flat field correction (not available at the time of commissioning), nor background subtraction. Then we used our own specific procedures for subtracting the background and reference star images. There was no further treatment to remove the glow stick effect other than background subtraction. Contrasts were measured azimuthally as a function of the angular separations first in the raw coronagraphic image (azimuthal mean), and then with the subtraction of a reference image (azimuthal standard deviation). We warn the reader that the contrast curves presented here are meant for comparison with simulated data and to demonstrate the capacity of the MIRI coronagraphs, and it would be overly optimistic to use them to assess the detectability of exoplanets, which would require accounting for the coronagraph's field transmission as well as the contrast definition proposed in Mawet et al. (2014). The reference-subtracted image was created either by subtracting a single reference exposure from the target exposure (one-to-one subtraction) or by subtracting an image constructed from a combination of multiple reference exposures (PCA subtraction). In commissioning, we used the SGD mode for both the target and the reference, so we have nine images for each, which means 81 possible one-to-one subtractions and nine PCA subtractions. We only display the resulting contrast curve that takes the best value of the contrasts for each separation independently (consistent with the best subtraction producing

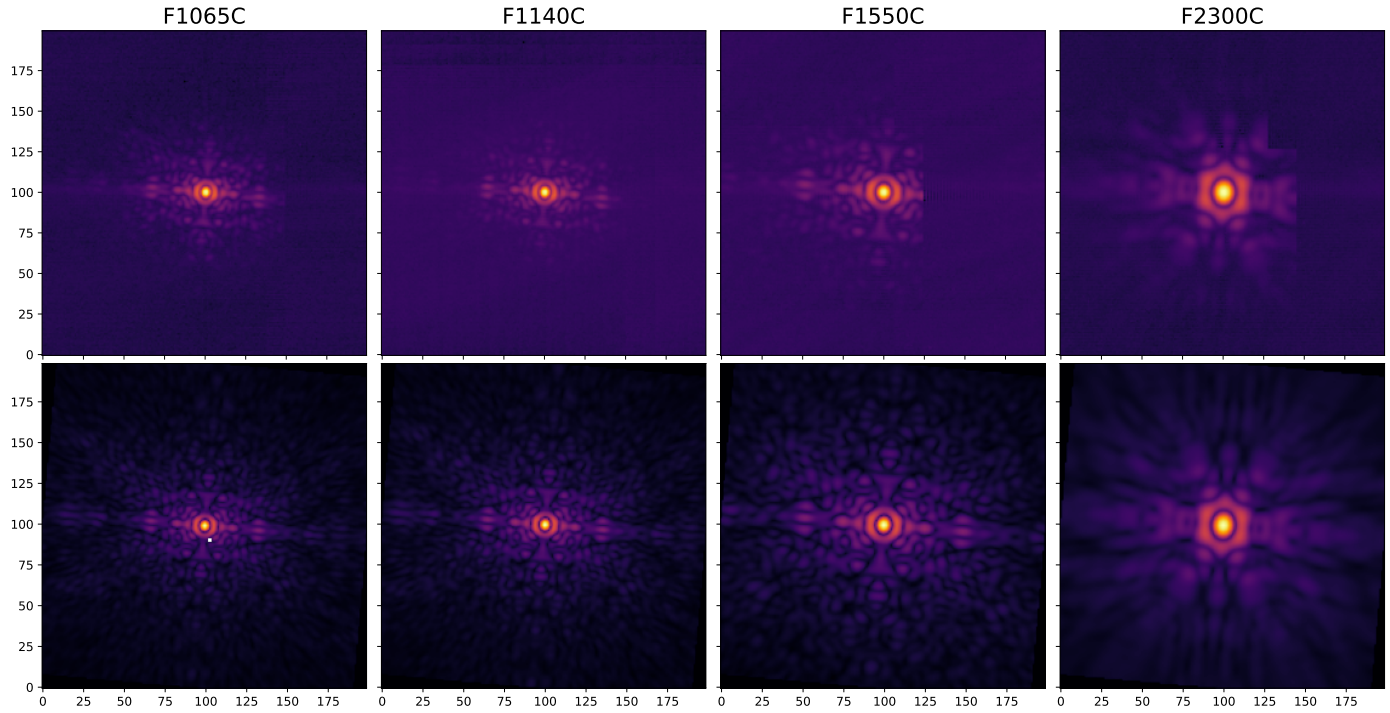

Fig. 2. Observed (*top*) versus simulated (*bottom*) PSFs (off-axis) in the four coronagraphic filters. The pixel scale is 110 mas. Some PSFs are cropped by the edges of the coronagraph's mechanical support. Simulated data use the nominal scenario (see Table 3). The intensity scale is not linear.

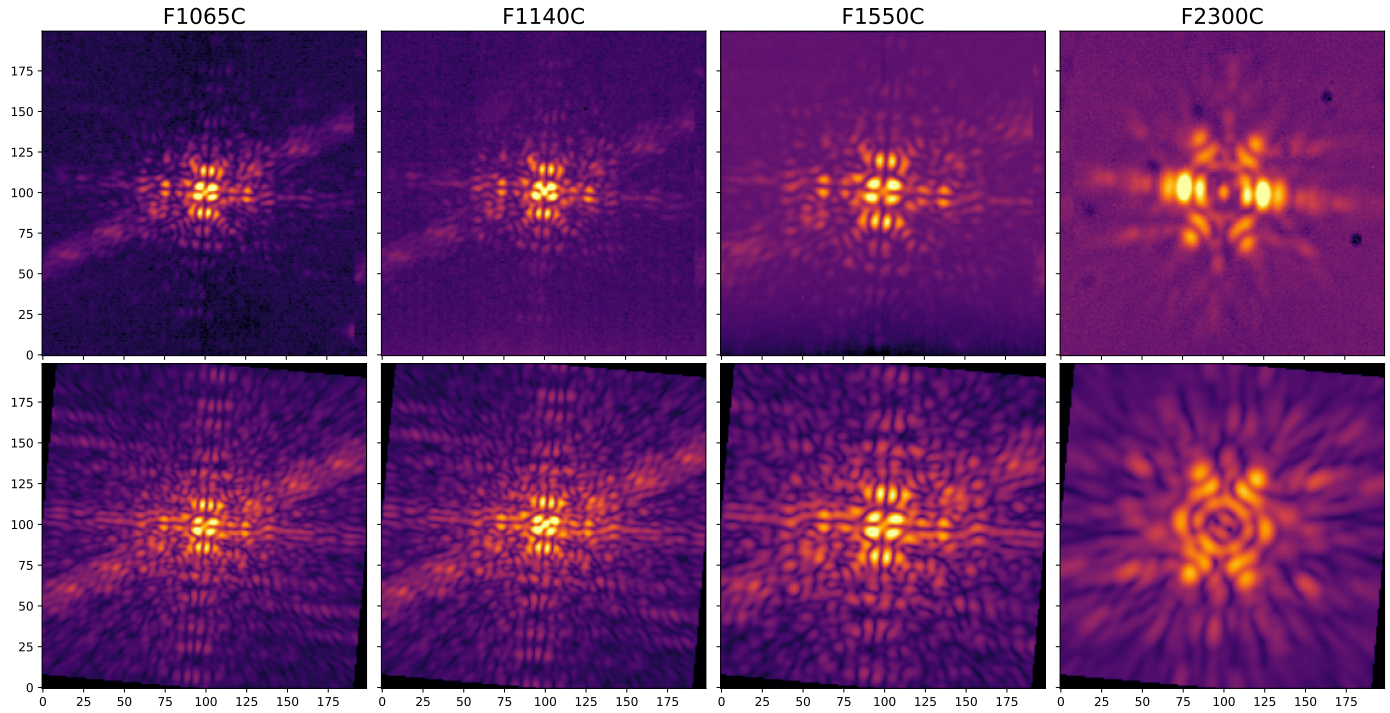

Fig. 3. Observed (*top*) versus simulated (*bottom*) coronagraphic images (on-axis) in the four coronagraphic filters. The pixel scale is 110 mas. Dark spots in the F2300C image correspond to background stars recorded during the background observation. Simulated data use the nominal scenario (see Table 3). The intensity scale is not linear.

the largest contrast at all separations). Examples of the subtracted images for the three 4QPMs are given in Fig. 4. The measurements are compared to the noiseless simulated contrasts for the three scenarios mentioned in Sect. 3, and to the Exposure Time Calculator (ETC) estimations using the actual flux of the observed stars and exposure times, together with a "medium background" configuration. The ETC assumes that the reference star subtraction is limited by photon and detector noises and so does not capture a possible variability in the optical wavefront aberrations or pointing.

Figure 5 displays the contrast curves for all four coronagraphic filters. The raw contrasts (brown lines) are in good agreement with the simulations of the 4QPMs coronagraphs. The F1065C and F1550C show the characteristic dip in the center,

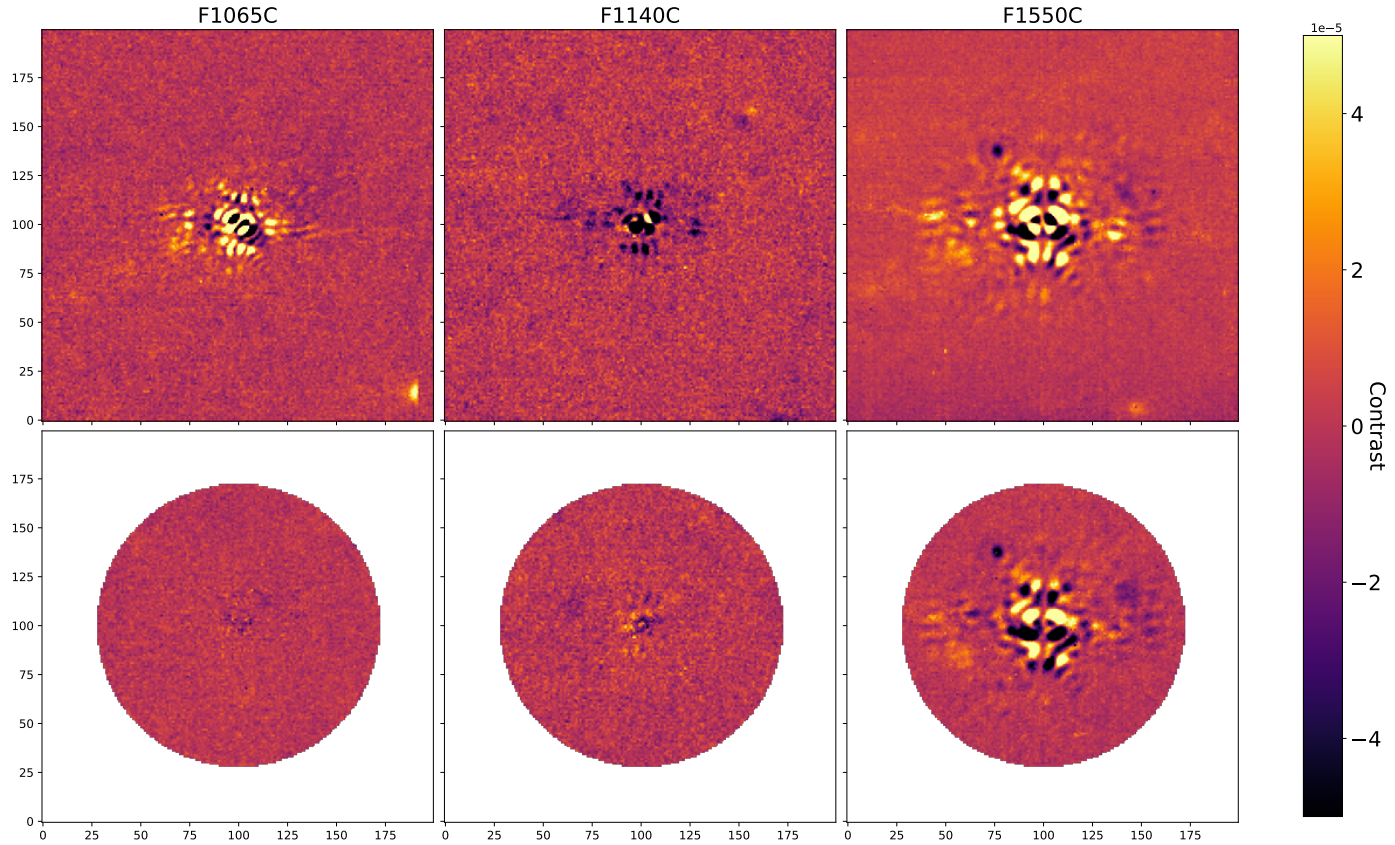

Fig. 4. One-to-one (*top*) versus PCA (*bottom*) subtraction of coronagraphic images (TARG and REF1) in the three 4QPM filters. Several background sources (either positive or negative) are observed around the target and reference stars. The pixel scale is 110 mas.

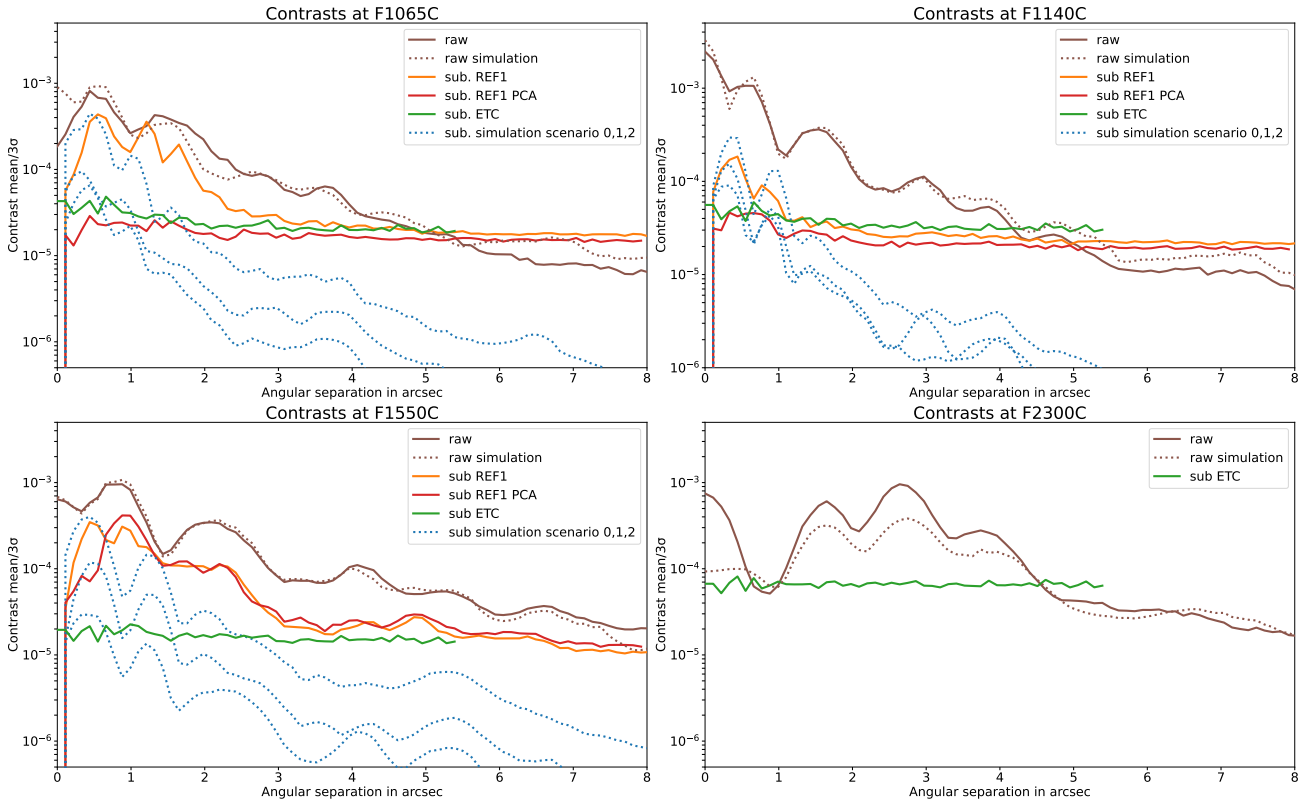

Fig. 5. Measured raw and 3σ reference-star-subtracted contrasts for all MIRI coronagraphic filters as compared to the simulations and to the ETC prediction. Subtracted contrasts are shown for the one-to-one and PCA algorithms. Reference stars were not observed at F2300C.

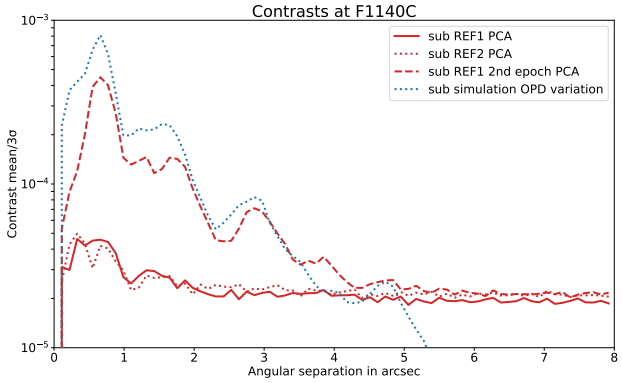

Fig. 6. Measured 3σ reference-star-subtracted contrasts with PCA in the F1140C filter for the single-epoch and two-epoch cases, and compared to the simulation that takes the wavefront error maps (OPD) into account before and after re-phasing of the primary mirror segments.

while the central region with F1140C is clearly affected by the chromatic leakage. Raw contrasts are usually better than $\sim 10^{-3}$ and reach the background limit at $\sim 10^{-5}$ (beyond 6″ or so). The one-to-one subtraction (orange lines) only provides a small gain with respect to the residual diffraction left behind the coronagraph, while PCA (red lines) offers a more substantial attenuation, reaching the background floor at all angular separations in F1065C and F1140C, which is in line with ETC expectations (green lines). The two references (REF1 and REF2 in Fig. 6) observed in F1140C back-to-back with the target produce very comparable contrast limits (dotted red line), indicating a small dependence with telescope slew (at least for a slew amplitude lower than 4 ∼ 20°). In the case where we applied PCA using the reference star observed 11 days later (REF1 second epoch in Fig. 6), the contrast significantly degrades (dashed red line). We interpret it as a result of telescope re-phasing during this time frame. At the end of May 2022, a micro-meteorite impacted segment C3, causing a significant departure of the wavefront with respect to the initial state. The first part of the F1140C observations (TARG, REF1, and REF2) were observed in this configuration with approximately 86 nm RMS of aberrations in total on the primary mirror, while the second epoch of REF1 was obtained after mirror re-phasing, leading to a reduced amount of 65 nm RMS aberrations. Such a difference is not visible in the raw coronagraphic images when comparing the two epochs. However, the reference-star-subtracted contrast in PCA if using these two epochs is reduced by as much as an order of magnitude at a separation of 0.66″ compared to the case with a single epoch. The overall contrast is affected up to a distance of about 4″. We retrieved the wavefront measurements bracketing these data, assigning the first map to the target and the second to the reference, in order to model the loss of contrast. We obtained almost the same contrast curve as the one measured (blue dotted line compared to red dashed line in Fig. 6), lending credibility to our hypothesis.

Overall, for F1065C and F1140C, PCA subtraction using reference stars achieves a contrast of $2–4.10^{-5}$ inside 1″. This is compatible with the best case scenario in the noiseless simulation, showcasing the very good performance met by the observatory in terms of pointing, repeatability, and stability. In fact, we estimate that the main parameters defining the reference-star-subtracted contrast are even better than the best case, with a line of sight jitter likely in the 1–2 mas range and TA at a level of 5 mas in total. A qualitative comparison with simulated images indicates a pupil shear of about 2–3% (responsible for the strip at ∼45° as seen in the coronagraphic images in Fig. 3). This value will be refined for each coronagraph configuration in Baudoz et al. (in prep.).

In the F1550C filter, the raw contrasts are in perfect agreement with the simulation, but both the one-to-one and the PCA subtraction are much worse than the ETC or simulated predictions. The 3σ contrast achieves only $\sim 4.10^{-4}$ at 1″, while we could expect 2.10^{-5}. Since the starlight rejection by the 4QPMs itself is coherent with the model, the only plausible explanation is again a mismatch in terms of wavefront errors between the target and the reference star. In fact, a "tilt event" (change in segment position; see Rigby et al. 2022) on one of the primary mirror segments presumably occurred between June 16 and June 19, 2022, and could be the cause of such a reduced contrast, although the causality cannot be firmly established. The project has committed to making telescope wavefront measurement available on roughly 2-day centers, which could determine if it is plausible that such an event occurred. There is currently no approach for more accurately locating the time of a tilt. With time, building a library of reference star images will certainly help mitigate these issues. We note that the very first science observations at F1550C in Carter et al. (2022) deliver reference-star-subtracted contrast within expectations.

Finally, we obtained a raw contrast measurement with the F2300C Lyot mask. We find that the level of contrast qualitatively matches the model prediction but does not agree perfectly. The discrepancy can be as large as a factor of 2–3 between 2″ and 3″ (if we omit distances that are inside the mask and hence irrelevant). The observed image itself features a stronger diffraction in the direction perpendicular to the bar holding the Lyot spot, producing an asymmetrical image in contrast to the simulation (Fig. 3). The reason for this disagreement is still under investigation, but we can confidently assume that, like the other coronagraphs, the Lyot mask performance will be set by the background level when using a reference subtraction. In fact, this is even more the case at F2300C since the background is stronger. Indeed, while the exposure times are similar in F1550C and F2300C, the achievable contrast is ∼4 times worse with the Lyot mask (as predicted with ETC).

5. Conclusion

Commissioning observations were the first opportunity to actually measure the performance of the MIRI coronagraphs in real conditions because high contrast imaging was not practical during the ground testing phase. The pointing accuracy and reproducibility have proved excellent, meeting the specifications of 5 mas at best, and definitely less than 10 mas (one-tenth to one-twentieth of a pixel). All four coronagraphs, the 4QPMs and the Lyot, behave satisfactorily on point sources, in the sense that the coronagraphic images and the raw contrasts are almost identical to the models and meet the contrast specifications. A small difference is found with the Lyot mask, for which an additional diffraction is superimposed on the predicted image, perpendicular to the bar. Calibrating the residual diffraction left unattenuated by the 4QPMs with reference stars brings the contrast to the limit imposed by thermal background and detector noises, at least for the two shortest wavelength filters, F1065C and F1140C. The reference-star-subtracted contrast with the F1550C filter is likely limited by variations in the wavefront errors of the primary mirror, which may have occurred during the observations (a tilt event). Similarly, subtracting images taken a few days apart shows significant deterioration of the contrast due to primary

mirror re-phasing between the two epochs. At the moment, it is recommended that each coronagraphic observation with MIRI include: a background image of the same duration as the science exposure, a nine-point SGD on the reference star (the five-point SGD was not tested during commissioning), and an off-axis image of the star for photometric calibration purposes, in agreement with former recommendations in JDox[2]. Alternatively, one can use the TA images for photometry, but they are obtained with different filters (usually a neutral density filter).

The commissioning of the MIRI coronagraphs reported here has demonstrated: excellent performance; that the use of the 4QPM technique provides the expected small IWA; and rejection factors and sensitivity in excess of pre-launch expectations. We can therefore anticipate that, with the observing recommendations in this paper, the MIRI coronagraphs will have a key role in the direct imaging of exoplanets to constrain atmospheric properties for the very first time at mid-IR wavelengths, as has already been illustrated with the very first release of an exoplanet image with a MIRI coronagraph by Carter et al. (2022).

Acknowledgements. The work presented is the effort of the entire MIRI team and the enthusiasm within the MIRI partnership is a significant factor in its success. We would like to thank Scott Rhorbach for his invaluable assistance and modelling to resolve the cause of the glowsticks issue, and the JWST and MIRI commissioning teams for their support in the execution of MIRI commissioning. The following National and International Funding Agencies funded and supported the MIRI development: NASA; ESA; Belgian Science Policy Office; Centre Nationale d'Etudes Spatiales (CNES); Danish National Space Centre; Deutsches Zentrum fur Luft-und Raumfahrt (DLR); Enterprise Ireland; Ministerio De Economiá y Competividad; Netherlands Research School for Astronomy (NOVA); Netherlands Organisation for Scientific Research (NWO); Science and Technology Facilities Council; Swiss Space Office; Swedish National Space Board; and UK Space Agency. MIRI draws on the scientific and technical expertise of the following organizations: Ames Research Center, USA; Airbus Defence and Space, UK; CEA-Irfu, Saclay, France; Centre Spatial de Liège, Belgium; Consejo Superior de Investigaciones Cientficas, Spain; Carl Zeiss Optronics, Germany; Chalmers University of Technology, Sweden; Danish Space Research Institute, Denmark; Dublin Institute for Advanced Studies, Ireland; European Space Agency, Netherlands; ETCA, Belgium; ETH Zurich, Switzerland; Goddard Space Flight Center, USA; Institute d'Astrophysique Spatiale, France; Instituto Nacional de Técnica Aeroespacial, Spain; Institute for Astronomy, Edinburgh, UK; Jet Propulsion Laboratory, USA; Laboratoire d'Astrophysique de Marseille (LAM), France; Leiden University, Netherlands; Lockheed Advanced Technology Center (USA); NOVA Opt-IR group at Dwingeloo, Netherlands; Northrop Grumman, USA; Max Planck Institut für Astronomie (MPIA), Heidelberg, Germany; Laboratoire d'Etudes Spatiales et d'Instrumentation en Astrophysique (LESIA), France; Paul Scherrer Institut, Switzerland; Raytheon Vision Systems, USA; RUAG Aerospace, Switzerland; Rutherford Appleton Laboratory (RAL Space), UK; Space Telescope Science Institute, USA; Toegepast-Natuurwetenschappelijk Onderzoek (TNOTPD), Netherlands; UK Astronomy Technology Centre, UK; University College London, UK; University of Amsterdam, Netherlands; University of Arizona, USA; University of Bern, Switzerland; University of Cardiff, UK; University of Cologne, Germany; University of Ghent; University of Groningen, Netherlands; University of Leicester, UK; University of Leuven, Belgium; University of Stockholm, Sweden; Utah State University, USA. A portion of this work was carried out at the Jet Propulsion Laboratory, California Institute of Technology, under a contract with the National Aeronautics and Space Administration.

References

Baudoz, P., Boccaletti, A., Riaud, P., et al. 2006, PASP, 118, 765
Boccaletti, A., Baudoz, P., Baudrand, J., Reess, J. M., & Rouan, D. 2005, Adv. Space Res., 36, 1099
Boccaletti, A., Lagage, P. O., Baudoz, P., et al. 2015, PASP, 127, 633
Carter, A. L., Hinkley, S., Kammerer, J., et al. 2022, AAS Journals, submitted ArXiv e-prints [arXiv:2208.14990]
Cavarroc, C., Amiaux, J., Baudoz, P., et al. 2008a, SPIE Conf. Ser., 7010, 70100W
Cavarroc, C., Boccaletti, A., Baudoz, P., Amiaux, J., & Regan, M. 2008b, PASP, 120, 1016
Choquet, E., Pueyo, L., Hagan, J. B., et al. 2014, Proc. SPIE, 9143, 914357
Danielski, C., Baudino, J.-L., Lagage, P.-O., et al. 2018, AJ, 156, 276
Hinkley, S., Carter, A. L., Ray, S., et al. 2022, PASP, 134, 1039
Lajoie, C.-P., Soummer, R., Pueyo, L., et al. 2016, Proc. SPIE, 9904, 99045K
Lebreton, J., Beichman, C., Bryden, G., et al. 2016, ApJ, 817, 165
Lightsey, P., Atkinson, C. B., Clampin, M. C., & Feinberg, L. D. 2012, Opt. Eng., 51, 011003
Mawet, D., Milli, J., Wahhaj, Z., et al. 2014, ApJ, 792, 97
Rieke, G. H., Wright, G. S., Böker, T., et al. 2015, PASP, 127, 584
Rigby, J., Perrin, M., McElwain, M., et al. 2022, ArXiv e-prints [arXiv:2207.05632]
Rouan, D., Riaud, P., Boccaletti, A., Clénet, Y., & Labeyrie, A. 2000, PASP, 112, 1479
Soummer, R., Pueyo, L., & Larkin, J. 2012, ApJ, 755, L28
Soummer, R., Lajoie, C.-P., Pueyo, L., et al. 2014, SPIE Conf. Ser., 9143, 91433V
Stolker, T., Quanz, S. P., Todorov, K. O., et al. 2020, A&A, 635, A182
Wagner, K., Boehle, A., Pathak, P., et al. 2021, Nat. Commun., 12, 922
Wright, G. S., Wright, D., Goodson, G. B., et al. 2015, PASP, 127, 595

[2] https://jwst-docs.stsci.edu/jwst-mid-infrared-instrument/miri-observing-strategies/miri-coronagraphic-recommended-strategies